Results from tests on matrices of lead tungstate crystals using high energy beams

J.P. Peigneux, M. Schneegans, E. Bateman, S. Burge, D. Cockerill, J. Connolly, B. B.N. Smith, R. Stephenson, E. Auffray, D. Barney, et al.

EUROPEAN ORGANIZATION FOR NUCLEAR RESEARCH

CERN-PPE/95-197
14 December 1995

Results from tests on matrices of lead tungstate crystals using high energy beams

J. P. Peigneux, M. Schneegans
LAPP, Annecy, France

E. Bateman, S. Burge, D. Cockerill, J. Connolly, B. Smith, R. Stephenson
Rutherford Appleton Laboratory, Didcot, U. K.

E. Auffray, D. Barney, I. Dafinei, P. Lecoq, T. S. Virdee*
CERN, Geneva, Switzerland

J. L. Faure, A. Givernaud, E. Locci, P. Verrecchia
Saclay, Gif-sur-Yvette, France

J. Barney, W. Cameron, D. Clark, D. Miller, C. Seez, M. Williams
Imperial College of Science Technology and Medicine, London, U.K.

R. Rusack
University of Minnesota, Minneapolis, U. S. A.

J. Bourotte, M. Haguenauer
LPNHE, Ecole Polytechnique, Palaiseau, France

M. Korzhik
Institute of Nuclear Problems, Minsk, Belarus

G. Alexeev, V. Katchanov, M. Oukhanov, P. Shagin, A. Singovsky
IHEP, Protvino, Russia

P. Denes
University of Princeton, Princeton, U. S. A.

T. Fluegel, D. Renker
Paul Scherrer Institute, Villigen, Switzerland

Submitted to Nuclear Instruments and Methods A

* Also at Imperial College of Science, Technology and Medicine, London, U.K.

Abstract

The performance of lead tungstate crystals using photomultipliers and Si avalanche photodiodes to detect the scintillation light has been studied using high energy electron, pion and muon beams at CERN. Results from tests carried out in 1993 and 1994 are presented. Good energy resolution has been obtained using photomultipliers. Some further development is required of crystals and avalanche photodiodes in order to achieve a performance, with avalanche photodiode readout, similar to that obtained using photomultipliers.

1. Introduction

The physics process that imposes the strictest performance requirements on the electromagnetic calorimeter at the LHC is the intermediate mass Higgs decaying into two photons [1]. The natural width of the Higgs boson in the intermediate-mass ($m_Z < m_H < 2m_Z$) region is small, and the observed width of a $H \rightarrow \gamma\gamma$ signal will be entirely dominated by the instrumental two-photon mass resolution. Thus the benchmark against which the performance of the electromagnetic calorimeter (ECAL) is measured is the two-photon mass resolution. The mass resolution has terms that depend on the resolution in energy (E_1,E_2) and the two photon angular separation (θ) and is given by

$$\frac{\sigma_M}{M} = \frac{1}{2}\left[\frac{\sigma_{E_1}}{E_1} \oplus \frac{\sigma_{E_2}}{E_2} \oplus \frac{\sigma_\theta}{\tan(\theta/2)}\right], \quad (1)$$

where $\oplus$ denotes a quadratic sum, E is in GeV and θ is in radians. The energy resolution is usually parameterized as

$$\frac{\sigma_E}{E} = \left[\frac{a}{\sqrt{E}} \oplus b \oplus \frac{\sigma_N}{E}\right], \quad (2)$$

where a is the stochastic term, b the constant and σ_N is the energy equivalent of electronic noise. At high luminosity σ_E/E will contain a contribution from pileup which adds to the electronic noise. In order to achieve a good energy resolution all the contributing terms have to be kept small at the relevant photon energies of $\approx$ 50 GeV.

For the Higgs two-photon decay at the LHC the angular term in the mass resolution (Eqn. 1) can become important and, at high luminosity, it may be necessary to measure the direction of the photons using information from the calorimeter alone.

Most fully active media, such as scintillating crystals, have the potential to achieve a stochastic term below 2%. The energy resolution is then limited by the control of systematics that build up the constant term. Achieving a constant term smaller than 0.5% for a large calorimeter is a challenging task. The CMS experiment has emphasized the benefit of a homogeneous ECAL since its inception and has tested several candidate media over the last few years. Amongst these are scintillating crystals, such as cerium fluoride (CeF_3) [2] and lead tungstate ($PbWO_4$) [3], and heavy scintillating glasses (hafnium fluoride HfF_4) [4]. The properties of these are compared in Table 1. The properties of BGO, pure CsI and BaF_2 are also shown for comparison.

The CMS collaboration has chosen lead tungstate crystals as the active medium for the electromagnetic calorimeter. Some of its desirable characteristics are:

i) a very short radiation length (0.9 cm) so that the volume needed to construct an electromagnetic calorimeter is relatively small,

ii) a small Moliere radius ($\approx$ 2 cm). About 80% of the electromagnetic shower energy is contained in a crystal with lateral dimensions of 2×2 cm^2 and a depth of 25 X_0 for particles incident at the centre of the crystal. This allows a reduction in the size of the area used for energy measurement thus reducing the energy pileup at high luminosities.

ii) fast scintillation light (80% of the light is captured in a gate of 25 ns as compared with that collected in a gate of 1 μs) and,

iii) some full size crystals have been shown to be radiation hard up to doses of 10 Mrad.

The calorimeter will sit in a 4T solenoidal magnetic field. In a high transverse magnetic field the scintillation light has to be detected by Si photodiodes or Si avalanche photodiodes (APDs) [5]. The latter can provide gain (< 100) in the presence of high magnetic fields.

The scintillation mechanism in lead tungstate is severely quenched and hence a sizable temperature variation of the light yield is expected. The measured variation of the light yield with temperature is $\approx -1.9\%/^\circ$C at room temperature [3, 6]. The gain of APDs is also temperature dependent. For example, at room temperature and a gain of 50, a gain variation of 0.3% results

from a temperature change of 0.15 °C or a bias voltage change of 60 mV for the Hamamatsu S5345LC low capacitance APDs .

Table 1. A comparison of the properties of scintillating crystals and glasses.

Property		BGO	Pure CsI	BaF_2	CeF_3	$PbWO_4$	HfF_4 Glass
Radiation length	cm	1.12	1.85	2.06	1.68	0.89	1.6
Moliere radius	cm	2.3	3.5	3.4	2.6	2.0	2.8
Density	g/cm^3	7.13	4.51	4.89	6.16	8.28	6.0
Small sample light yield	γ/MeV	4000	1500	8500	2000	140	165
τ (short)	ns	300	6	0.9	9	≤10	8
(long)	ns		35	630	30	36	25
% Light in 25 ns			85	25	50	80	70
Peak wavelength (fast)	nm	480	310	220	300	450-500	325
(slow)			420	300	340		
Temp. dependence (fast)	%/°C	−1.6	−0.6	0	0.15	−1.9	− 0.4
of light yield (slow)	%/°C			− 2.0			
Index of refraction		2.15	1.95	1.5	1.62	2.2	1.5

This paper is organized as follows: Section 2 gives the details of the two matrices of $PbWO_4$ crystals exposed to the high energy beams. Section 3 discusses Si avalanche photodiodes and their use. Section 4 outlines briefly the beamlines and the data taken. Section 5 describes the results, and conclusions are drawn in Section 6.

2. Description of $PbWO_4$ Test Matrices

2.1 Test Matrix I

The first matrix, used in 1993, consisted of 21 parallelepiped crystals with lateral dimensions of 20 × 20 mm^2 and differing lengths (Table 2). They were mounted so that the front faces were flush, with longer crystals protruding back into the box containing the front-end electronics. This was done to ease the task of injecting light into crystals via optical fibres for the purpose of monitoring. Each crystal was wrapped with 150 μm of reflecting millipore paper and 30 μm of aluminized mylar.

The scintillation light was detected by Hamamatsu S3590-03 Si photodiodes with an active area of 10 × 10 mm^2. The preamplifiers were modified versions of those used with vacuum triodes in the OPAL endcap lead glass calorimeter [7]. The shaping time was set to be 30 ns. The silicon photodiodes were glued onto the crystals with Dow Corning 3145 RTV adhesive/sealant optical compound with a refractive index of 1.41. A short run was also made with one Hamamatsu S5345 high capacitance Si avalanche photodiode with an active diameter of 5 mm.

In this exploratory test the temperature of the crystals was not stabilized.

The photoelectron yield for the central nine crystals was measured using muons traversing the crystals and the Si photodiodes. The most probable signal for a minimum ionizing particle traversing a 300 μm thick Si detector is ≈ 25,000 electrons. The smallest trigger scintillator was large enough in area that some triggering muons did not traverse the diode. The pulse height spectrum for one crystal is shown in Fig. 1. The energy calibration obtained from 80 GeV electron

runs gives 8.0 ADC counts/GeV for the crystal shown in Fig. 1. The energy is summed over nine crystals. It is assumed that ≈ 80% of this energy is deposited in the crystal struck at the centre. From this it can be calculated that the yield of photoelectrons is 6.7 p.e./MeV. A light yield of 38 photons/MeV is estimated assuming that the diode covered 25% of the rear face (the rest of the face was left bare) and that the diode had a mean quantum efficiency of ≈ 70% at the relevant wavelengths. The photoelectron yield for the central nine crystals ranges from 6.7k to 11.2 k p.e./GeV (or 38-64 γ/MeV) and is tabulated in Table 2. We assign an error of about 20% on these figures though the relative error should be considerably smaller.

Table 2 : Some parameters of the $PbWO_4$ Test Matrix I.

	18 cm	18 cm	18 cm	
18 cm	18 cm 10.2 p.e. 1.9 k	20 cm 8.1 p.e. 1.9 k	18cm 11.1 p.e. 2.2 k	18 cm
18 cm	20 cm 8.9 p.e. 2.4 k	22.5 cm 6.7 p.e. 2.0 k	20 cm 9.0 p.e. 2.3 k	18 cm
18 cm	22 cm 8.9 p.e. 2.2 k	20 cm 11.2 p.e. 2.3 k	18 cm 9.9 p.e. 2.2 k	18 cm
	18 cm	18 cm	18 cm	

Key	Length of crystal Photoelectron yield (p.e. / MeV using Si PIN Diodes) Electronics noise at the output of the preamplifier/shaper (in electrons)

2.2 Test Matrix II

The second matrix, used in 1994, consisted of 35 tapered crystals (truncated pyramids) with nominal front face dimensions of 18 × 18 mm^2, rear face dimensions of 21.5 × 21.5 mm^2 and a nominal length of 214 mm. Each crystal was wrapped in Tyvek-90 paper of a thickness of ≈ 150 μm. Prior to the beam test the light yield and the longitudinal uniformity of the crystals were measured. The non-uniformity was defined as $NU = (LY_{max}–LY_{min})/LY_{min}$ where LY_{max} was the light yield measured in a region 5 cm from the rear and LY_{min} is the minimum light yield.

The crystals were mounted on a base plate as shown in Fig. 2. The front fixture enabled light to be injected into the crystals via optical fibres. The assembly was placed in a custom built, insulated and light-tight enclosure and maintained at a stable temperature. Two schemes for temperature stabilization were used, one employing air at a fixed temperature, forced through the enclosure, and another employing water circulating through copper plates which were in contact with the outer surface of the crystal matrix. The latter scheme provided a more stable temperature whereas the former did not deliver enough cooling and there was a residual day-night variation of

temperature of about 2 °C. The enclosure was placed on a platform that enabled translation and rotation of the test matrix. The crystal array was positioned so that the inner faces of the crystals lay on a spherical surface with a radius of 1.46 m, close to the eventual situation expected in CMS at η=0.

The scintillation light was detected by low capacitance Hamamatsu Si avalanche phototodiodes (S5345LC) and later by Phillips PM1911 photomultipliers. The photodetectors were coupled to the crystals with optical grease (Oken 6262A, n=1.42 at $\lambda \approx 450$ nm). The useful area of the photodetectors amounted to 4.3 % and 38 % of the crystal rear surface for the APDs and PMs respectively. As the remainder of the rear face was left bare we assume that the fraction of the emerging light collected was the same as the fractional area covered.

Table 3 : Some parameters of the $PbWO_4$ Test Matrix II.

20.9 cm 1.0 13 %	21.2 cm 1.4 7 %	21.8 cm 1.0 9 %	21.5 cm 1.1 7 %	22.1 cm 0.8 12 %	Al dummy
21.2 cm 1.6 5 %	21.3 cm 1.4 5 %	21.4 cm 1.0 3 % **T8**	21.1 cm 1.4 4 %	21.7 cm 1.1 14 %	21.3 cm 14 %
20.4 cm 1.2 9 %	21.5 cm 1.1 2 %	21.4 cm 1.4 1 % **T14**	21.4 cm 1.2 5 %	22.6 cm 1.1 11 %	21.3 cm 13 %
21.8 cm 0.9 9 %	21.7 cm 1.1 3 %	21.7 cm 1.1 3 %	22.2 cm 1.2 3 %	21.5 cm 0.8 10 %	21.5 cm 12 %
21.6 cm 1.2 7 %	22.1 cm 1.1 6 %	21.6 cm 0.9 9 %	20.1 cm 1.2 8 %	21.6 cm 1.2 9 %	21.5 cm 2 %
20.9 cm 1.1 11 %	21.2 cm 1.4 8 %	21.0 cm 1.6 7 %	21.9 cm 1.0 8 %	21.4 cm 1.2 14 %	21.6 cm 19 %

Key	Length of crystal Relative light yield (Unity corresponds to $\approx$ 50 γ/MeV) Longitudinal non-uniformity of the crystal

The front-end electronics chain (pre-amplifier, shaper and line driver) were specifically designed to minimize the electronics noise for the given characteristics of the APDs. The preamplifiers were AC coupled to the APDs with CR-RC shaping time of 35 ns. Each amplifier was calibrated by applying a negative step function to a 1 pF capacitor at the APD signal node. The accuracy of the relative calibration was limited by the 10% spread in the capacitances of the test capacitors. The signal was sent over 80m of RG58 cable and split in the ratio 1/8:7/8 before integration in independent channels by LeCroy FERA 11 bit ADCs with a 150 ns gate. The pulse

shape of the signal before entering the ADC is shown in Fig. 3. Temperature probes were embedded in each front-end assembly and in contact with the respective APD package.

Data were also taken with a preshower detector consisting of one detector plane of Si strips with a pitch of 2 mm preceded by a variable number of 4 mm lead plates. The preamplifiers were those used with the Si photodiodes in the Test Matrix I.

The light yield of $PbWO_4$ crystals is too low to enable the use of conventional Si PIN photodiodes to detect the scintillation light from high energy electrons without inducing significant tails in the energy distributions (see Section 5.1). A photodevice with gain and a small response to ionizing radiation (r.i.r.) is necessary. Si avalanche photodiodes (APDs) can provide modest gain and have a smaller r.i.r. than Si PIN diodes. The main tests in 1994 were made using Si APDs to detect the scintillation light.

3. Silicon Avalanche Photodiodes

Recent developments in avalanche photodiode design have led to their consideration as replacements for photomultipliers [5]. APDs can provide gain and are insensitive to high magnetic fields in any orientation. APDs are reverse biased diodes with an internal field high enough ($> 10^5$ V/cm) that electrons and holes acquire sufficient energy to generate further electron-hole (e-h) pairs by impact ionization, yielding avalanche gain. The gain mechanism depends strongly on the applied electric field and the device temperature.

The structures of the three APDs tested are shown in Fig. 4. Incident photons convert in the first part of the p layer. The resulting electrons are accelerated in the high field p-n junction region and generate further e-h pairs. Below a certain field strength holes are not able to generate e-h pairs. The electrons are collected at the back contact. In the EG&G APD the electrons are collected after drift in the π-region. For incident charged particles the electrons (from e-h pairs) created in the p region undergo multiplication whereas those created in the n and π regions do not.

Avalanche multiplication is a random process which leads to an additional fluctuation in the collected charge characterized by an excess noise factor, F. The r.m.s. broadening of a signal from n photoelectrons is given by $\sigma = \sqrt{(F/n)}$. The coefficient a in Eqn. 2 then becomes

$$a = a_{intr} \oplus \sqrt{\frac{F}{N_{pe}}}$$

where a_{intr} also contains contributions to the stochastic term other than that due to finite photostatistics and N_{pe} is the number of photoelectrons/MeV. Typical APDs have $F \approx 2$.

To first order the energy equivalent of electronics noise, σ_N (see Eqn. 2), at the output of the APD, can be expressed as

$$[\sigma_N\,(\mathrm{MeV})]^2 = C^2 \frac{4kT}{g_m} \frac{1}{\tau\,(e.M.N_{pe})^2} + t\,.\,e\,\left[\frac{I_{ds}+M^2.I_{db}.F}{4(e.M.N_{pe})^2}\right]$$

where e is the electric charge, M the avalanche gain, I_{ds} is the component of dark current that is not amplified (surface leakage current), I_{db} is the component of dark current that is amplified (bulk leakage current), τ is the shaping time, k is Boltzmann's constant, T is the absolute temperature, g_m is the first stage transconductance, t is the integration gate time and C is the total parallel capacitance.

The detailed APD requirements for our application are :

• the p layer should be thick enough to absorb most of the incident light in the relevant wavelength range. The wavelength range of the scintillation light of $PbWO_4$ is 400 - 600 nm. In this range the photon absorption length in Si varies from 0.1 μm to ≈ 2 μm. However the thickness of this layer has to be kept thin enough to minimise the response to ionizing radiation and keep small the bulk leakage current (I_{db}) which undergoes multiplication. The bulk leakage current becomes sizable if the APD suffers significant radiation damage.

• the electric field in the avalanche region should be large enough to allow multiplication by electrons but small enough not to allow significant hole multiplication. The size and the shape of the electric field in this region determines the excess noise factor F.

• the size of the drift region should be large enough for a low capacitance device but small enough to keep low the response to ionizing radiation and the bulk leakage current.

A good design of an APD for electromagnetic calorimetry at the LHC is therefore a compromise between the various opposing requirements. We consider below the details of Hamamatsu and EG&G APDs.

The APDs manufactured by Hamamatsu are made by epitaxial growth on a silicon substrate. The impurity concentrations and types can be accurately controlled during this process and thus diodes with suitable doping profiles can be made. When under bias the depletion region extends across the full width of the epitaxial layer. The standard 5 mm diameter APD made by Hamamatsu (Fig. 4a) has a capacitance of 325 pF suggesting that the total thickness of the device is around 7 - 8 μm. The photo-conversion layer is estimated to have a thickness of ≈ 2 μm. Any charge produced in this layer undergoes the full gain whereas the charge produced uniformly in the avalanche region undergoes an average of half of the full gain. Hence the effective thickness of Si, $t_{eff}(Si)$, for the charged particle traversal will be ≈ (2 + 5/2) μm = 4.5 μm which is consistent with the measurements described below. The low capacitance APD has a thicker p layer (see Fig. 4b). This had the undesirable consequence of increasing the size of r.i.r. to a level found later to be unacceptable. Another undesirable feature of the low capacitance Hamamatsu devices was a high surface leakage current.

The EG&G APDs are manufactured by ion implantation using thin wafers of crystalline silicon. The internal structure is such that the avalanche region, with a thickness of ≈ 5 μm, is located behind the photo-conversion region with a thickness of ≈ 2 μm (Fig. 4c). When the APD is fully biased the depletion region extends right through the wafer with the result that the device capacitance is much lower than the Hamamatsu APDs. The capacitance of the 5 x 5 mm^2 device is ≈ 25 pF suggesting an overall thickness of ≈ 100 μm. These devices have a smaller $t_{eff}(Si)$ than the low capacitance Hamamatsu APDs but larger than the high capacitance ones due to the contribution from the ≈ 90 μm thick drift region. This contribution amounts to the thickness of the drift region divided by the gain. The surface leakage current of the EG&G APDs is considerably smaller than that of Hamamatsu ones. However preliminary measurements indicate that the excess noise factor for these diodes is larger than that measured for the Hamamatsu devices.

Low capacitance Hamamatsu APDs were used in the beam tests described in Section 5.2.2. The r.m.s. of the electronics noise, referred to the input, as a function of voltage for one APD is shown in Fig. 5 [8]. Also shown are the gain and noise referred to the output. The running condition selected corresponded to a gain of ≈ 25. The voltages on all the APDs were set to give this value of gain. The voltage required was found using low energy X-rays which convert in the active region of the APD and deposit a known amount of charge. Ag K_α radiation was used for the gain optimization. For the calibration procedure a ^{55}Fe source, capable of producing a signal simultaneously in all the APDs, was used. A 5.9 keV X-ray leads to the creation of 1640 electrons in silicon so permitting the gain of the APD to be estimated.

An important parameter of the APDs is the size of the response to ionizing radiation. It can be quantified by expressing it in terms of the thickness of Si PIN diode required to give the same signal as that arising from the traversal of a charged particle in the APD. We have exposed three APDs and a 200 μm thick Si PIN diode to protons with a kinetic energy of 64 MeV in a beam at the Paul Scherrer Institute. The resulting pulse height spectra are shown in Fig. 6. An attenuation of 6 dB was applied to the signal from the low capacitance Hamamatsu APD. The results are given in Table 4. The effective thickness of Si, $t_{eff}(Si)$, is evaluated by

$$t_{eff}(Si)_{APDi} = \frac{200\mu m}{(\text{peak position})_{PIN}} \times \frac{(\text{peak position})_{APDi}}{M}$$

The values obtained for $t_{eff}(Si)$ for the various APDs can be understood by examining their internal structure.

Table 4 : Results from an exposure to 64 MeV protons of a Si PIN diode and different APDs.

	PIN Diode	Hamamatsu APD high capacitance	Hamamatsu APD low capacitance	E. G. & G. APD
Peak position# (arb.)	175	160	696*	273
Voltage (V)	20	146	288	280
Gain (M)	1	53	53	32.5
$t_{eff}(Si)$ at M=50 (μm)	200	3.5	15	8.6

pedestal subtracted.
* corrected for an attenuation of 6 dB

The various properties of the APDs tested are summarized in Table 5. R&D is being carried out with Hamamatsu to decrease the leakage current and the capacitance of their APDs without increasing $t_{eff}(Si)$. A decrease of the excess noise factor is sought for the EG&G devices.

Table 5. The parameters of the different photodevices.

Parameter	Si PIN Diode	EG&G	Hamamatsu (High C)	Hamamatsu (Low C)
Size [mm^2]	10 × 10	5 × 5	ϕ = 5 mm	ϕ = 5 mm
Capacitance [pF]	40	25	320	80
Leakage current * [nA]	≈ few	20	100-300	400-900
QE at 500 nm [%]	≈ 60	≈ 75	≈ 65	≈ 65
Photosensitive layer [μm]	≈ 2	≈ 2	≈ 2	≈ 2
Multiplication layer [μm]	none	≈ 6	≤ 6	≈ 25
1/M × dM/dT * [% per °C]	-	–3.5	–2.3	–2.5
1/M × dM/dV * [% per V]	-	2	15	4
Excess noise factor F *	1	2.8	2.0	2.1
t_{eff} (Si) (M=50) [μm]	200	8.6	3.5	15

* at a gain of M = 50 for APD

4. The Beamline and Data Taking

In 1993 the beam tests were carried out in the CERN H2 beamline and in 1994 in the CERN H4 beamline. We describe the layout of the latter beamline. Electrons in the momentum range from 10 GeV to 150 GeV were used. Data were also taken with 225 GeV muon and 80 GeV pion

beams. The detecting elements in the beam line included beam-defining trigger scintillation counters, a beam halo veto scintillator and four planes of drift chambers. The scintillators allowed the selection of "narrow" beam (4 x 4 mm^2) or "wide" beam (20 x 20 mm^2) triggers. Most of the data were taken with the 20 x 20 mm^2 trigger. Drift chamber information was used off-line to define smaller regions when needed. The drift chambers allowed the measurement of the position of incidence of the beam on the crystal front face to an accuracy of $\approx$ 300 μm. The incident flux was below $\approx$ 5000 particles per SPS spill (of a duration of $\approx$ 2 seconds). The beam momentum spread was defined by collimators which were set such that $\Delta p/p < 0.2\%$. *This spread is not unfolded in the results presented below.*

Tower to tower calibration was carried out using 50 GeV electrons. About 25k events were recorded for the calibration of each tower. A scan in energy was made with the beam centered successively in each of several towers. About 100k events were recorded at each energy. Data were also taken with 225 GeV muons at normal incidence and with the crystals rotated by 90° so that the muons traversed the crystals perpendicular to their long axes. The transverse scan muon data were used to investigate the longitudinal uniformity of light collection. To investigate electron-pion separation some 200k pion events were recorded.

5. Results

5.1 Results from Test Matrix I

Data were taken with incident electrons with momenta of 20, 40, 80 and 150 GeV/c, and with muons of 225 GeV/c in the H2 beam of the CERN SPS North Area.

The distribution of the energy summed over nine crystals for 150 GeV electrons is shown in Fig. 7. A long tail was observed on the high energy side of the spectra. This is due to charged particles passing through the 300 μm thick Si photodiodes. This was verified by placing a diode directly behind the one detecting the scintillation light. A long tail is observed when the pulse height distribution for the "light blind" diode is examined (Fig. 8). This diode did not see the scintillation light and the signal is due to the energy deposited by charged particles leaking out of the crystal at the end of the shower. The energy deposited in the blind diode can be used to correct for the signal observed in the light detecting diode. However the resolution expected from a crystal calorimeter cannot be attained as can be seen by the large width and the tails in the corrected pulse height distribution for 150 GeV electrons shown in Fig. 9. A cut on the signal in the blind diode can be used to obtain narrower distributions but at the price of a much lower efficiency for electrons. Data were also taken with differing thicknesses of lead in front of the crystals. The distribution of the sum of energy in nine crystals are shown in Fig. 10 for lead of thickness of 10 mm or 25 mm placed in front of the crystals. It can be seen that the high side tail is much reduced when 25 mm of lead is placed in front of the crystals but the width increases considerably.

The tails on the high energy side result from the fact that the direct response of the Si photodiodes to ionizing radiation leaking from the rear of the crystal is significant compared with the scintillation light. For this reason an attempt was made to detect the scintillation light using Si APDs. A 5 mm diameter Hamamatsu Si APD was mounted on the rear of an 18 cm long crystal. In Fig. 11 the pulse height distributions obtained from an 18 cm long crystal with a Si APD, to detect the scintillation light, are compared with those from a 20 cm long crystal using a photomultiplier and an 18 cm crystal with Si photodiode. It is evident that the high energy side tail in Fig. 11c almost disappears due to the smaller response of the APDs to ionizing radiation.

It was decided to make further tests in 1994 with a matrix of longer crystals using Si APDs to detect the scintillation light.

5.2 Results from Test Matrix II

5.2.1 Response to muons and electrons using photomultipliers

The temperature of the setup using PMs as photodetectors was stabilized by water cooling. The stability attained was ± 0.2 °C over the period of the run (≈ 20 hrs). This is shown in Fig 12.

The longitudinal uniformity of the response of the crystals was measured by firing muons transverse to the long axis of crystals. This is shown in Fig. 13 for Tower 8.

The calibration constants were deduced by two methods: one using a minimization procedure and the other using 50 GeV electrons shot in the centre of each crystal. In the minimization procedure the calibration coefficients of a 3×3 array of crystals, used to reconstruct the energy when an electron was incident in the central crystal, were obtained by minimizing the width of the energy distribution. Both methods give results that are consistent with each other. The reconstructed energy distributions for electrons with energies of 35 and 150 GeV, incident over almost the whole face of the central crystal, are shown in Fig. 14. The energy is summed in 9 crystals centered on Tower 14. A tail on the low energy side is observed especially for the higher energies. This is due to longitudinal energy leakage and longer crystals are therefore needed. The energy resolution measured using PMs is shown in Fig. 15. The line corresponds to the parameterization

$$\frac{\sigma}{E} = \frac{3.5\%}{\sqrt{E}} \oplus 0.35\%$$

The dispersion in the beam momenta has not been unfolded. For comparison the effect on energy resolution of limited shower containment in the 3 × 3 array of crystals was studied using GEANT. The resulting parameterization leads to $\sigma/E \approx 2.25\%/\sqrt{E} \oplus 0.26\%$. The test beam results show that an energy resolution of ≈ 0.5% can be obtained at high energies. In the measurement the dominant contribution to the stochastic term is from limited photostatistics. It is estimated that about 2500 photoelectrons / GeV were detected by the photomultiplier for Tower 14. The PM covered about 35% of the rear face of the crystal and had an emission spectrum weighted quantum efficiency of ≈ 12% .

5.2.2 Response to electrons, muons and pions using APDs

These tests were carried out using low-capacitance Hamamatsu APDs.

Energy equivalent of electronics noise

The width of the sum of pedestals of 9 crystals was used to establish the energy equivalent of the electronics noise. It was found to be ≈ 250 MeV corresponding to about 75 MeV per crystal. The introduction of a preshower detector in the same enclosure as the crystals led to an increase in the electronics noise to ≈ 350 MeV for nine crystals but only ≈ 90 MeV/crystal indicating that there was a sizable amount of correlated noise. This did not improve very much once the preshower was removed. Due to insufficient beam time we did not investigate the cause of this increase.

Response to ionizing radiation

Muons with an energy of 225 GeV were fired uniformly into the front face of Tower 14. The hit pattern of muons depositing more than 600 MeV in the crystal is shown in Fig. 16. With the 600 MeV cut there is a higher density of impacts in the area covered by the APD. This is due to the energy deposited by the muons traversing the APD. The size of the response to ionizing radiation can be determined from the distribution shown in Fig 17. The first peak, at ≈ 300 MeV, is due to the scintillation light produced by muons traversing only the crystal whereas the second peak, at

≈ 1.2 GeV, is due to muons that also go through the APD. Hence the most probable energy that a minimum ionizing particle deposits in the APD is equivalent to 900 MeV.

The photoelectron yield can be deduced from the above numbers once the internal structure of the APD is known. The measurements described in Section 3 indicate an effective diode thickness of 13 μm of Si. This leads to a photoelectron yield of ≈ 1200 p.e./GeV. This is consistent with the value deduced from the test pulse.

Temperature stability

Forced air cooling was employed during the test using APDs as photodetectors. The temperature stability achieved was poor. A typical trace of the variation of temperature is shown in Fig. 18 and the day-night cycle can clearly be seen. This complicated the task of energy calibration as the calibration runs were not necessarily taken at the same temperature as the runs used in the study of energy resolution. For this reason the minimization procedure for the study of energy resolution was preferred. The electron data runs were of very short duration and during them the temperature changed by less than 0.05 °C. These results are consistent with those when the temperature corrections are properly taken into account (see later).

The influence of changing temperature on the response of the crystals to 50 GeV electrons was studied during a twenty hour run [9]. Fig 19 shows the variation of the measured response versus temperature. The temperature was measured only on the outer surfaces of the matrix. The thermal diffusion time results in a time lag between the temperature measured at the crystal surface and that deep in the crystal. The system as a whole, including the APDs, shows a time-lag of about 2.1 hours between the maximum of the measured temperature and the minimum of the response. When allowance is made for this time-lag a temperature coefficient of –2.2%/ °C is obtained.

Response to electrons

Electrons of momenta 20, 35, 50, 80 and 120 GeV/c were fired in the centre of Tower 8. The distribution of the measured energy in 9 crystals, centered on Tower 8, is shown in Fig. 20a for electrons with an energy of 120 GeV. The electrons were incident uniformly over an area of 3×3 mm^2 at the centre of Tower 8. The tail on the high energy side is due to particles leaking out of the rear of the crystals and into the APD. This hypothesis was verified by placing a preshower detector with 16 mm of lead in front of the crystals (Fig. 20b). Table 6 quantifies the effect of placing 16 mm (2.9 X_0) of lead in front of the crystals. The size of the tail is considerably reduced since the flux of particles leaking out of an e.m. shower is decreased by the increased length of the calorimeter. In order to reduce the size of such tails it is clearly desirable to :

- increase the light detected by the APDs by increasing the light generation and light collection,
- increase the length of the crystals,
- design APDs that have a smaller response to ionizing radiation.

The EG&G and the high capacitance Hamamatsu APDs are respectively about a factor of 2.5 and 4 less sensitive to charged particles than those used in our tests (see Table 5).

Table 6: The percentage of events with energy $E \geq \langle E \rangle + 2\sigma(E)$.

Energy		80 GeV	120 GeV	120 GeV with 16mm Pb preshower
Area of impact	3 x 3 mm^2	14.4 %	18.5 %	10.6 %
	full area	9.4 %	10.8 %	6.9 %
Gaussian resolution σ/E (%)		0.87 %	0.79 %	0.71 %

The energy resolution measured using the minimization method is shown in Fig. 21. The line corresponds to the parameterization

$$\frac{\sigma}{E} = \frac{6\%}{\sqrt{E}} \oplus 0.5\%$$

The dispersion in the beam momenta has not been unfolded. The energy equivalent of electronics noise, amounting to ≈ 250 MeV, has been subtracted from the measured width in order to display the stochastic term (given by the slope of the line shown in Fig. 21) and the constant term (given by the offset at 1/E=0). The difference between the stochastic terms for the APD and PM readouts is due to smaller photostatistics and a larger excess noise factor for the APDs. The central crystal (Tower 8) used in the measurements with APDs had a light yield which was lower by 30 % compared with that from the central crystal (Tower 14) used in tests with PMs. The APDs covered only ≈ 5% of the rear face of the crystals and had a quantum efficiency of ≈ 65%. It is estimated that about 900 photoelectrons/GeV were detected. The excess noise factor F is large for the APDs (F ≈ 2 – 3) and a stochastic term around 5%, i.e. $\sqrt{(F/900)}$, is therefore expected. In order to reduce the size of the stochastic term to the value found in the data using photomultipliers, an increase, by a factor of at least three, is required in the product of light generation, light collection and light conversion. A lower value of the F would also help. Further R&D is being carried out to improve the crystal quality, increase the light yield and reduce F.

The energy resolution was also measured using the calibration constants obtained from 50 GeV electron beam runs in the nine crystals. The measurement of the time-lag between the measured and the actual temperature of individual crystals was used to correct the crystal response [9]. Crystals 1-3, 7-9 and 13 -15 were calibrated by correcting and equalizing their response to 50 GeV electrons incident in a 2 x 2 mm^2 area in which the response of the crystal is the maximum. The measured energy resolution after temperature correction is shown in Fig. 22. The energy equivalent of the electronics noise has been subtracted from the measured energy resolution. These results are consistent with those shown in Fig. 21. The linearity of response for both the methods is found to be better than 1% over the range studied.

Position resolution

The small Moliere radius of lead tungstate results in narrow showers. A particle incident in the centre of a crystal with front face dimensions of 18 x 18 mm^2 will deposit ≈ 72% of its energy in that crystal. Nevertheless the energy deposited in the neighbouring eight crystals is large enough to enable measurement of the position of impact [10]. The centre of gravity, X_c, is defined as

$$X_c = \frac{\Sigma_{left} - \Sigma_{right}}{\Sigma_9}$$

where Σ_{left} and Σ_{right} refer to the summed pulse height in the column of three crystals to the left and to the right of the central crystal (Tower 8) and Σ_9 is the pulse height summed over all the nine crystals.

The beam telescope consisting of four layers of drift chambers was used to measure the position of incidence of the beam, labeled X_D. The variation of $X_c - X_D$ with X_c for 50 GeV electrons at normal incidence is shown in Fig. 23. However it is possible to apply a correction to X_c in order to make the mean value of $X_c - X_D$ zero at any given X_c. A look-up table is computed for each energy and a correction is obtained by interpolation. The distribution of the resulting position determination for 50 GeV electrons incident uniformly across the front face of Tower 8 is shown in Fig. 24. The position resolution as a function of energy is shown in Fig. 25. A linear least squares fit to the data yields the relationship

$$\sigma(X_c) = \frac{2.02 \pm 0.48}{\sqrt{E}} \oplus (0.29 \pm 0.06) \text{ mm.} \quad (E \text{ in GeV})$$

Electron charged-pion separation

The difference between the lateral and longitudinal development of electromagnetic and hadronic showers can be used to distinguish electrons from charged pions [11]. A charged hadron usually deposits only a fraction of its energy in the ECAL. Hence the difference between its momentum measured in the tracker and the energy measured in the e.m. calorimeter allows the separation of electrons from charged pions.

The electron pion separation was studied using 80 GeV electrons and pions. In the absence of a hadron calorimeter this study used only the energy deposits in the crystals. The energy spectrum as measured by a 3 x 3 array of crystals, for pions incident over Tower 14, is shown in Fig. 26. As expected the majority of pions deposit a small fraction of their energy in the calorimeter.

Two distinct types of cut were used to distinguish electrons from charged pions :

- an energy cut, E_{cut}, on energy deposited in the 3×3 array of crystals centred on the central crystal for an "E/p" measurement,
- a lateral shape cut, $S_{cut} = \frac{\Sigma_9 - E_c}{\Sigma_9}$, where Σ_9 is the energy in the 3 x 3 array and E_c is the energy in the central crystal.

The difference between the measured energy spectra for electrons and pions can be seen in Fig. 27. The distribution of the variable S_{cut} is shown in Fig. 28. for electrons and charged pions. For the electron runs there is a clear peak around $S_{cut} = 0.2$. This is consistent with the fact that an electron, incident in the centre of a crystal, will deposit around 77 % of the energy contained in 9 crystals, in the central crystal. The plot for pions is much flatter with a broad peak around $S_{cut} = 0.5$. Table 7 gives the electron identification efficiency and the pion rejection factors obtained for various choices of cuts.

Table 7: The electron identification efficiency and the pion rejection factors.

Energy Cut	S_{cut}	e^- events	π^- events	pion rejection factor	electron efficiency
none	none	85646	86763	1	100 %
$\pm 3\,\sigma$	none	80324	225	386	94 %
$\pm 3\,\sigma$	$0.18 < S_{cut} < 0.45$	77792	95	913	91 %

We expect some improvement in the pion rejection by using an APD with a smaller response to ionizing radiation.

5.2.3 Response to electrons in the presence of a preshower

Energy resolution

The energy deposited in the silicon detectors of the preshower can be used to correct for the energy lost in the lead placed in front of the crystals. The reconstructed energy, E_{rec}, is given by

$$E_{rec} = \alpha\, E_{presh} + \Sigma_9.$$

An example of the distribution of the reconstructed energy is shown in Fig. 20b. The energy resolution, as a function of incident electron energy, with and without correction is shown in Fig. 29. The line corresponds to the parameterization

$$\frac{\sigma}{E} = \frac{8.5\%}{\sqrt{E}}$$

The position resolution of the preshower

The transverse spread of the electromagnetic shower, after $\approx 3\ X_0$ of lead, is of the order of a few mm., which means that signals are seen in more than one silicon strip. This enables a centre-

of-gravity calculation to be performed. The relatively poor precision of the drift chambers and large amount of cross-talk present in the system prevented any effective "S curve" correction to be made. The distribution of the difference between the position of the incident electron measured by the beam chambers (X_D) and that measured by the preshower for 50 GeV electrons is shown in Fig. 30. The spatial precision at this energy is approximately 410 μm which is somewhat worse than previous measurements (≤ 350 μm [12]). Fig. 31 shows the measured spatial precision as a function of the reciprocal of the energy and is fitted by :

$$\sigma(X_p) = \frac{1.58 \pm 0.46}{\sqrt{E}} \oplus (0.36 \pm 0.06) \text{ mm}$$

It can be seen that the stochastic term is smaller than that found using crystals but the constant term is larger. This is probably due to the presence of noise and cross-talk.

Angular resolution

In principle the measurement of the angular resolution of the preshower-crystal system is simple : it is the spread of $X_c - X_p$ divided by the distance along the beam direction between the planes where the two measurements are made ($Z_c - Z_p$); Z_p is the position of the preshower plane and Z_c is, approximately, the position of the shower maximum. However Z_c is not known directly and must be estimated from data taken with particles incident on crystals at known angles. This measurement is complicated by the "S-curve" which is different when the beam is not at normal incidence. Fig. 32 shows how the "S-curve" (in this case it is a plot of $X_c - X_p$ versus X_p) changes with angle. The mean values of $X_c - X_p$ are shown as horizontal lines. It can be seen that the mean value of $X_c - X_p$ depends on the angle of incidence, and it is this mean divided by the angle in radians (small angles) which yields the lever-arm and thus the depth given by Z_c. Five runs, with angles of incidence between –5° and + 5°, were studied. A least squares fit was performed through the means (Fig. 33). The gradient determines the lever-arm. The lever arm is found to sit at 58.5 mm, which after the subtraction of 7.5 mm for the distance between the preshower and the front of the crystals, yields a depth of ≈ 5.7 X_0. If 2.85 X_0 for the lead of the preshower is added to this one obtains a depth of ≈ 8.5 X_0 corresponding roughly to the shower maximum for electrons with an energy of 50 GeV. The same depth is found from runs made with 2.1 X_0 of lead in front of the crystals.

Once the length of the lever-arm has been determined the angular resolution can be estimated by

$$\sigma_\theta = \frac{\sigma(X_c - X_p)}{\text{lever-arm}}$$

for small angles. Fig. 34 shows how the angular resolution depends on the incident energy of electrons. It is assumed that the distance between the preshower detector and the front face of the crystals is 4 cm as would be the case in the CMS barrel design. The angular resolution is fitted by

$$\sigma_\theta = \frac{36.5 \pm 6.5}{\sqrt{E}} \oplus (4.1 \pm 0.8) \text{ (mrad)}$$

6. Conclusions

The results presented here demonstrate that lead tungstate crystals are suitable for use in the CMS experiment at the LHC. The drawback of the low light yield of these crystals can be overcome by the use of relatively large area Si avalanche photodiodes. Development work is continuing to further improve the crystal characteristics such as the light yield, the radiation hardness and growth techniques, and the characteristics of the avalanche photodiodes such as the response to ionizing radiation, the excess noise factor and leakage current.

References

[1] C. Seez et al., Proc. of Large Hadron Collider Workshop, Vol. II, Aachen, 1990, eds. G. Jarlskog and D. Rein.

C. Seez and T. S. Virdee, CMS Internal Notes TN/92-56 (1992), TN/94-289 (1994),

[2] Status Report of RD18, "Crystal Clear Collaboration", CERN/DRDC/94-53, Jan. 1995.

[3] W. van Loo, Phys. Stat. Sol. 28 (1975) 227.

W. Moses and S. E. Derenzo, IEEE Trans. Nucl. Sci., NS-36 (1989) 173.

V. G. Baryshevsky et al., Nucl. Instr. and Meth. A322 (1992) 231.

T. S. Virdee, Proc. of IVth Intl. Conf. on Calorimetry in High Energy Physics, Isola d'Elba, Italy, 1993.

V. Katchanov, Proc. of IVth Intl. Conf. on Calorimetry in High Energy Physics, Isola d'Elba, Italy, 1993.

M. Kobayashi et al., Nucl. Instr. and Meth. A333 (1993) 429.

O. V. Buyanov et al., Nucl. Instr. and Meth. A349 (1994) 62.

[4] P. R. Hobson et al., RAL preprint RAL-P-95-003 (1995).

[5] E. Lorentz et al., Max Planck Institute Note MPI-PHE-93-23 (1993), Munich, Germany.

[6] I. Dafenei et al., Proc. of Symposium on Scintillating and Phosphor Materials, San Francisco, 1994.

P. Lecoq et al., CMS Internal Note CMS TN/94-308 (1994).

[7] R. Stephenson, RAL preprints RL82-082 (1982), RL83-075 (1983), RL87-019 (1987).

[8] J. E. Bateman et al., CMS Internal Note CMS TN/95-023 (1995).

[9] J. L. Faure et al., CMS Internal Note CMS TN/95-030 (1995).

[10] D. Barney, CMS Internal Note CMS TN/94-315 (1994).

[11] D. Barney, CMS Internal Note CMS TN/94-314 (1994).

[12] P. Aspell et al., CERN-PPE/95-151 (1995), submitted to Nucl. Instr. and Meth.

Figure Captions

Fig. 1 The pulse height spectrum for muons traversing a crystal.

Fig. 2 The layout of crystals.

Fig. 3 The shape of the signal due to electrons (after 80 m of cable).

Fig. 4 The internal structure of APDs; a) Hamamatsu - high capacitance, b) Hamamatsu - low capacitance and c) EG&G.

Fig. 5 The gain of a typical Hamamatsu low capacitance APD and the r.m.s. of the electronics noise in terms of electrons referred to the input and output of the preamplifier as a function of the bias voltage.

Fig. 6 The pulse height spectra due to 64 MeV protons in different photodetectors a) Si PIN photodiode, b) Hamamatsu APD - high capacitance, c) Hamamatsu APD- low capacitance and d) EG&G APD. The lower peak in the APD distributions is due to incident protons missing the APD.

Fig. 7 The distribution of energy for 150 GeV electrons using Si PIN diodes.

Fig. 8 The pulse height distribution for a light blind Si PIN diode.

Fig. 9 The distribution of ADC counts for 150 GeV electrons using the light blind diode to correct for the energy deposited by shower particles traversing the light detecting diode.

Fig. 10 The sum of energy in 9 crystals when lead of a thickness of a) 10 mm or b) 25 mm is placed in front of the crystals. Also indicated is the fraction of the events that are beyond the peak and outside the Gaussian curve.

Fig. 11 The pulse height distributions obtained from a) 20 cm long crystals using a photomultiplier to detect the scintillation light, b) an 18 cm crystal with Si photodiode and c) an 18 cm long crystal with a Si APD.

Fig. 12 The temperature stability of the setup cooled by water.

Fig. 13 The longitudinal uniformity of the response of crystals using muons.

Fig. 14 The reconstructed energy distribution for electrons with energies of 35 and 150 GeV incident over almost the whole face of the central crystal.

Fig. 15 The energy resolution measured using PMs.

Fig. 16 The hit pattern of muons depositing more than 600 MeV in crystal 14.

Fig. 17 The size of the response to ionizing radiation. The first peak is due to the scintillation light produced by muons traversing only the crystal whereas the second peak is due to muons that also go through the APD.

Fig. 18 A typical trace of the variation of temperature when forced-air cooling was used. The day-night cycle can clearly be seen. The line is to guide the eye.

Fig. 19 The variation of the measured response versus temperature.

Fig. 20 The reconstructed energy distribution for 120 GeV electrons: a) without and b) with a preshower detector. A correction has been applied for the energy lost in the lead.

Fig. 21 The energy resolution using the minimization method (see text). The line is to guide the eye.

Fig. 22 The measured energy resolution using the 50 GeV electron calibration runs. The calibration coefficients have been corrected for temperature variation.

Fig. 23 The variation of the difference between the position of incidence deduced from the crystals (X_C) and that from the beam drift chambers (X_D) versus X_C.

Fig. 24 The distribution of the position determined using crystals.

Fig. 25 The position resolution, deduced using the crystals, as a function of energy.

Fig. 26 The pion energy distribution measured using a 3×3 array of crystals with the beam incident on crystal 14.

Fig. 27 The measured energy spectra for 80 GeV electrons and pions.

Fig. 28 The distribution of the variable S_{cut}.

Fig. 29 The energy resolution as a function of energy with and without correction using the preshower signal.

Fig. 30 The distribution of the difference between the position of the incident electron measured by the beam chambers (X_D) and that measured by the preshower (X_p) for 50 GeV electrons.

Fig. 31 The position resolution of the preshower detector as a function of 1/E.

Fig. 32 The difference between the position measured using the crystals (X_c) and that using the preshower detector (X_p) versus X_c.

Fig. 33 The mean value of (X_c–X_p) versus the angle of incidence of electrons.

Fig. 34 The angular resolution as a function of the energy of electrons.

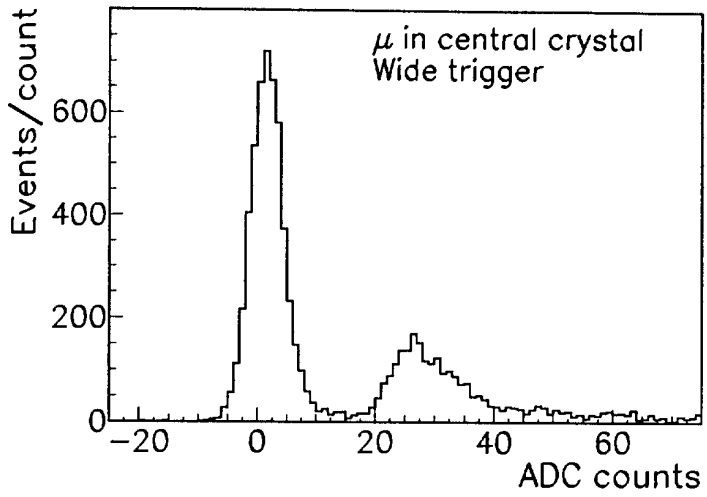
μ in central crystal
Wide trigger
Events/count
600
400
200
0
−20
0
20
40
60
ADC counts

Fig. 1

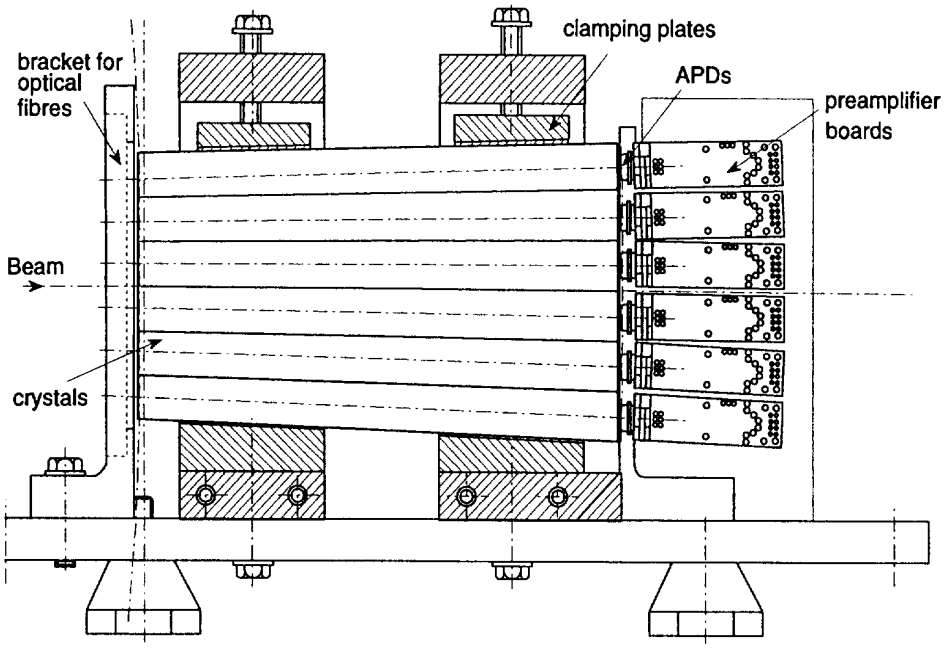
bracket for optical fibres
clamping plates
APDs
preamplifier boards
Beam
crystals

Fig. 2

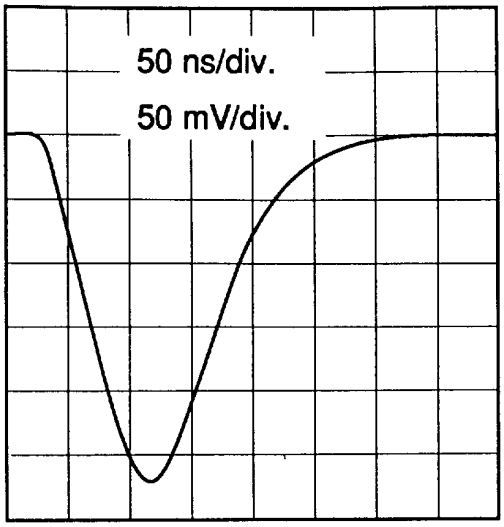

Fig. 3

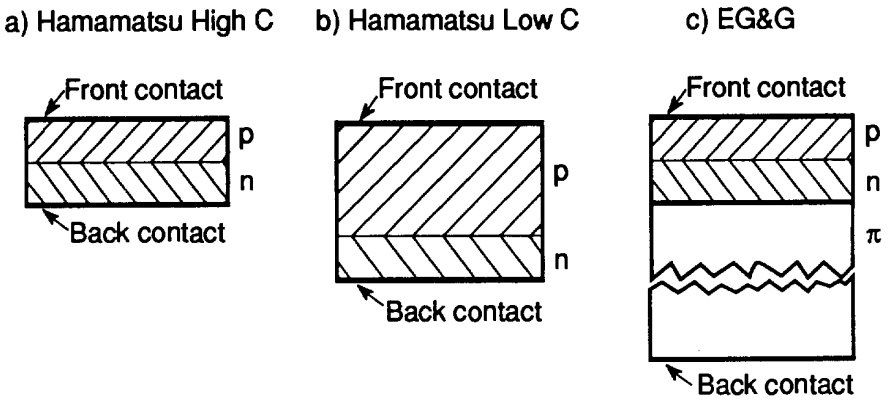

Fig. 4

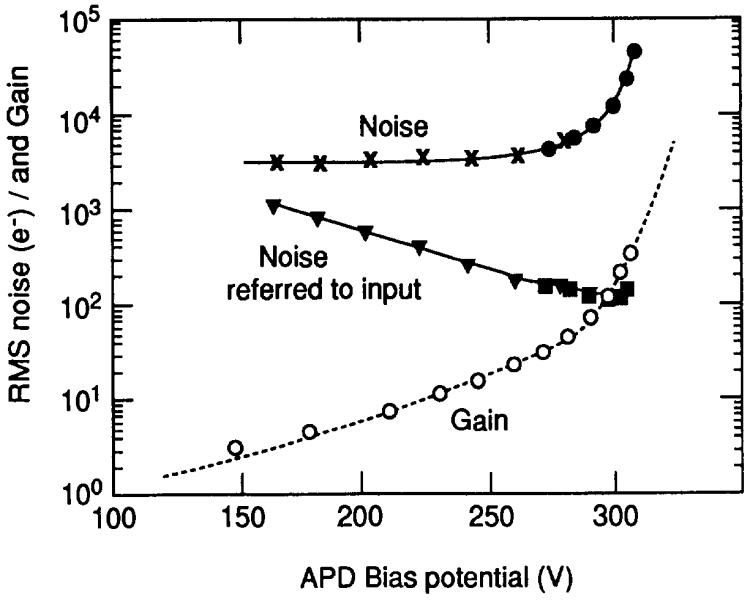

Fig. 5

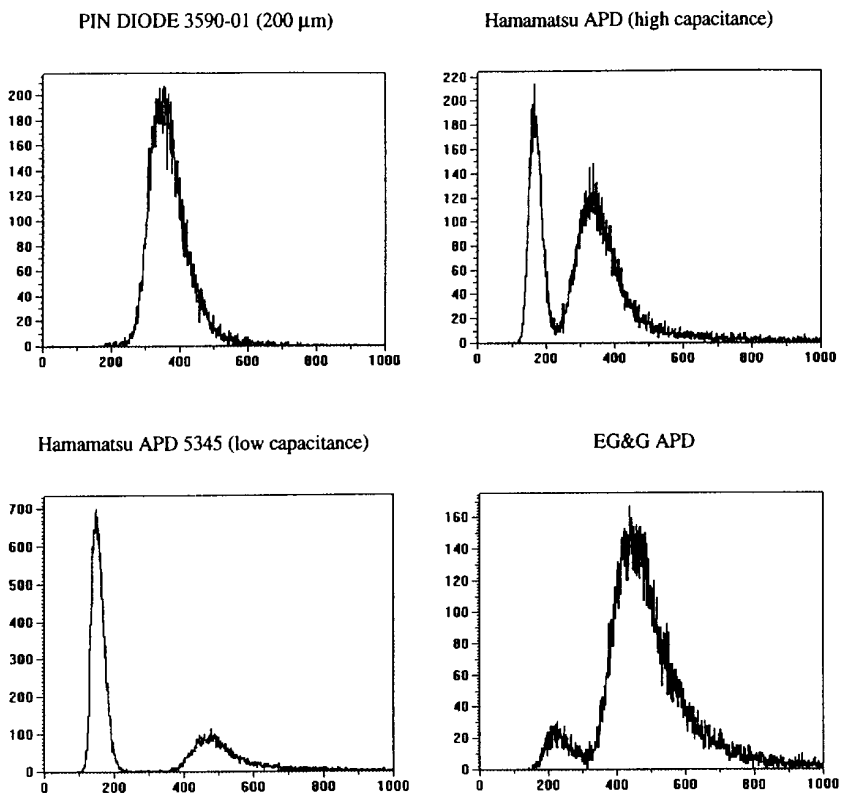
PIN DIODE 3590-01 (200 µm)
Hamamatsu APD (high capacitance)
Hamamatsu APD 5345 (low capacitance)
EG&G APD

Fig. 6

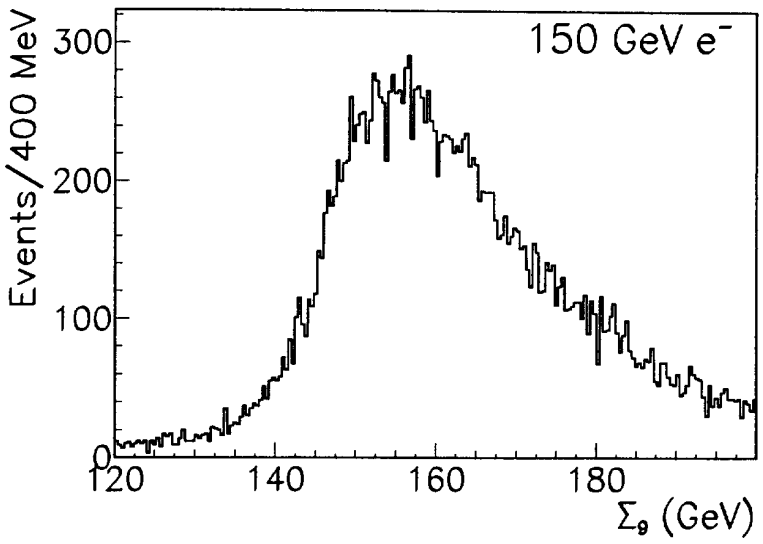
150 GeV e⁻
Events/400 MeV
300
200
100
0
120
140
160
180
Σ₉ (GeV)

Fig. 7

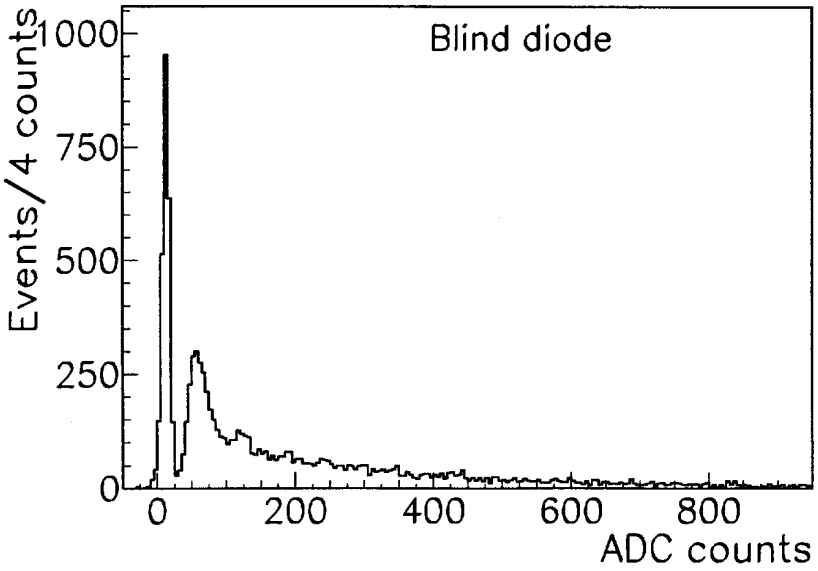
Blind diode
Events/4 counts
1000
750
500
250
0
0
200
400
600
800
ADC counts

Fig. 8

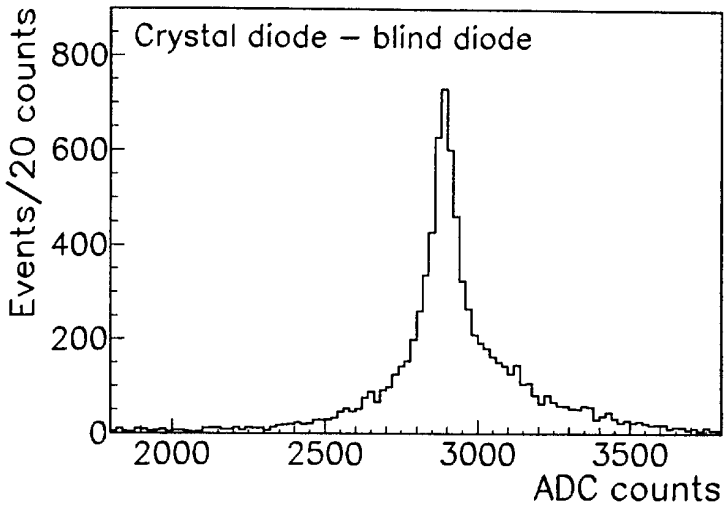

Fig. 9

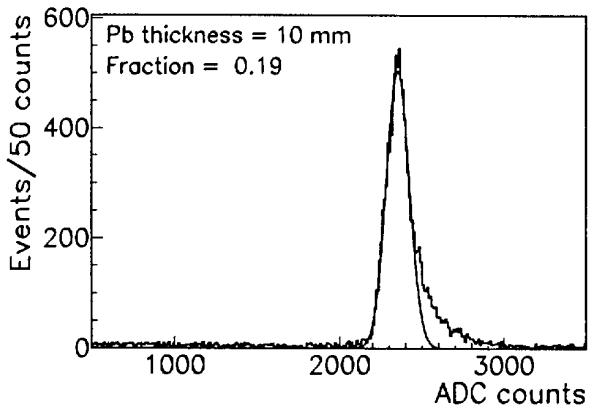

Fig. 10a

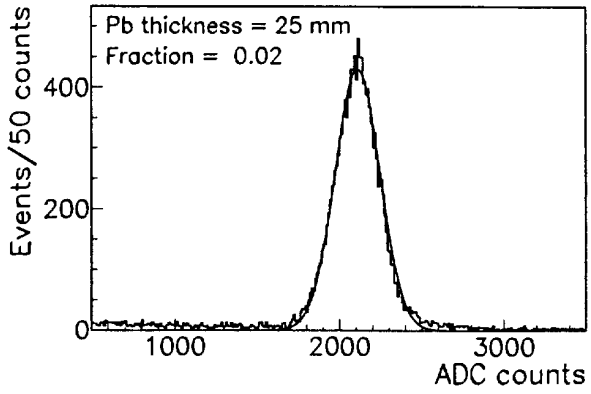

Fig. 10b

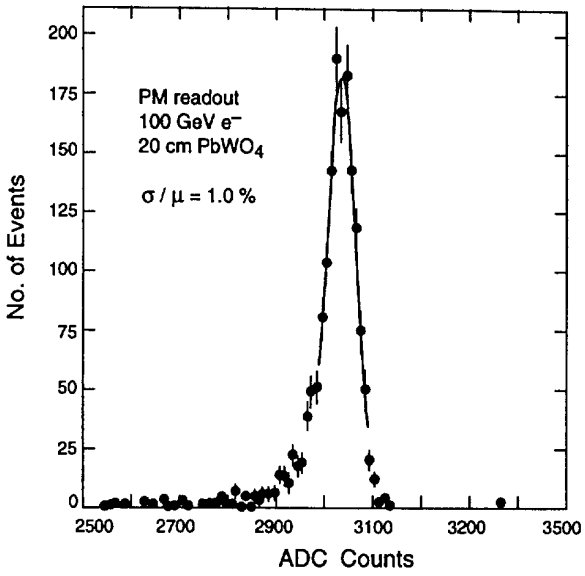

Fig. 11a

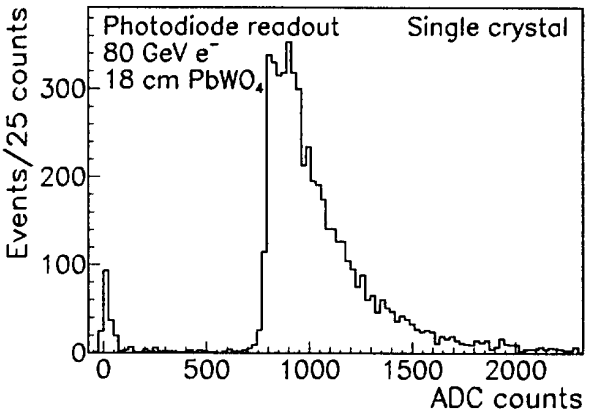

Fig. 11b

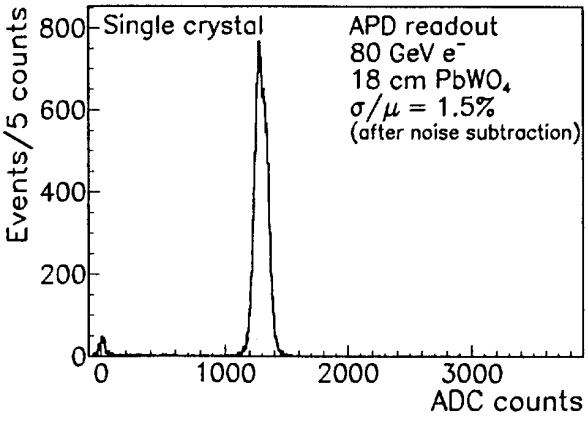

Fig. 11c

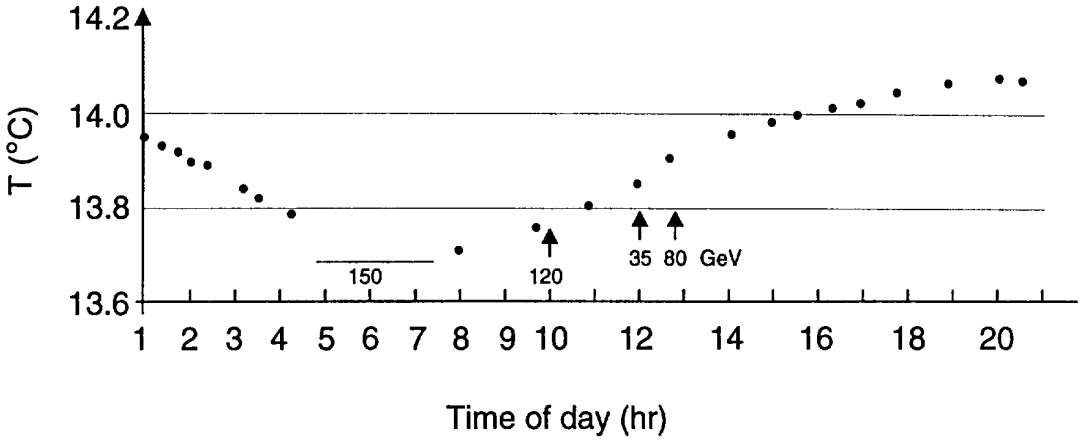
14.2
14.0
13.8
13.6
T (°C)
150
120
35 80 GeV
1 2 3 4 5 6 7 8 9 10 12 14 16 18 20
Time of day (hr)

Fig. 12

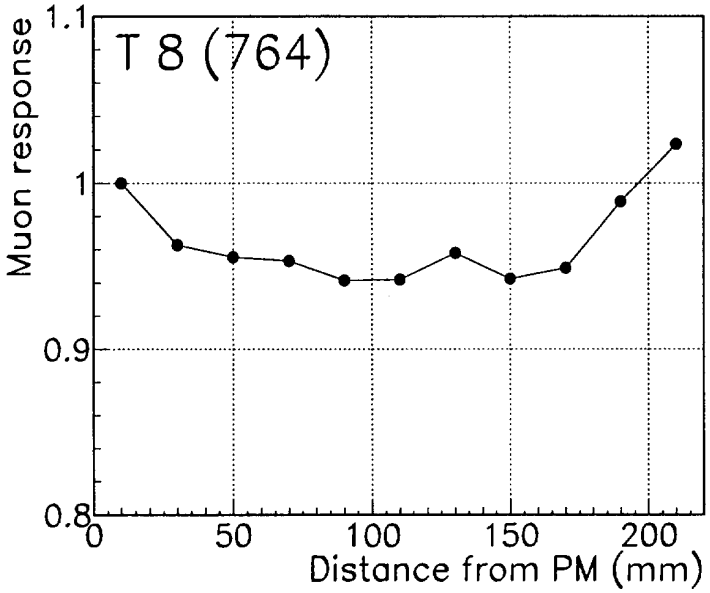
T 8 (764)
Muon response
1.1
1
0.9
0.8
0 50 100 150 200
Distance from PM (mm)

Fig. 13

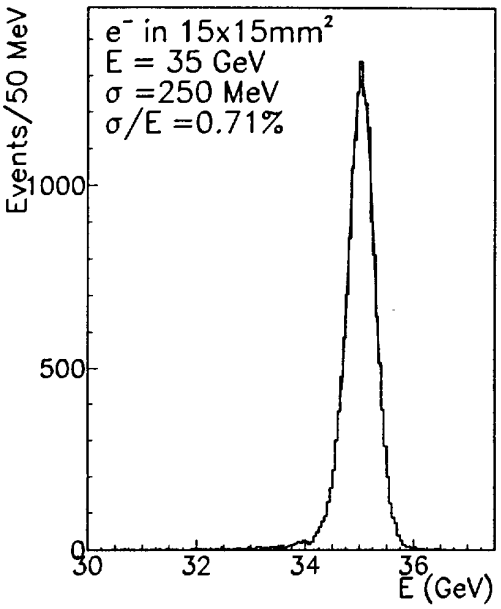

Fig. 14a

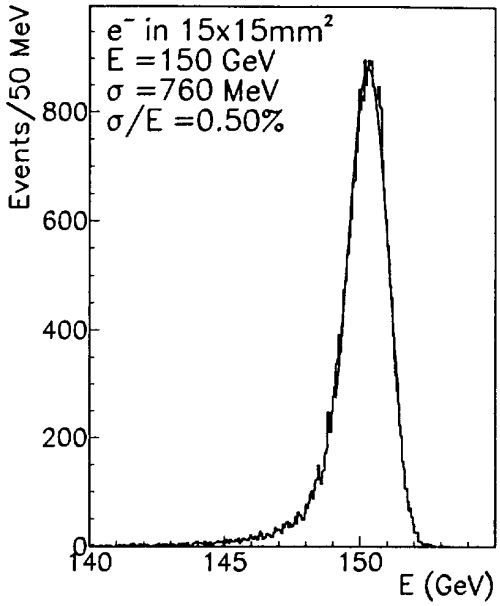

Fig. 14b

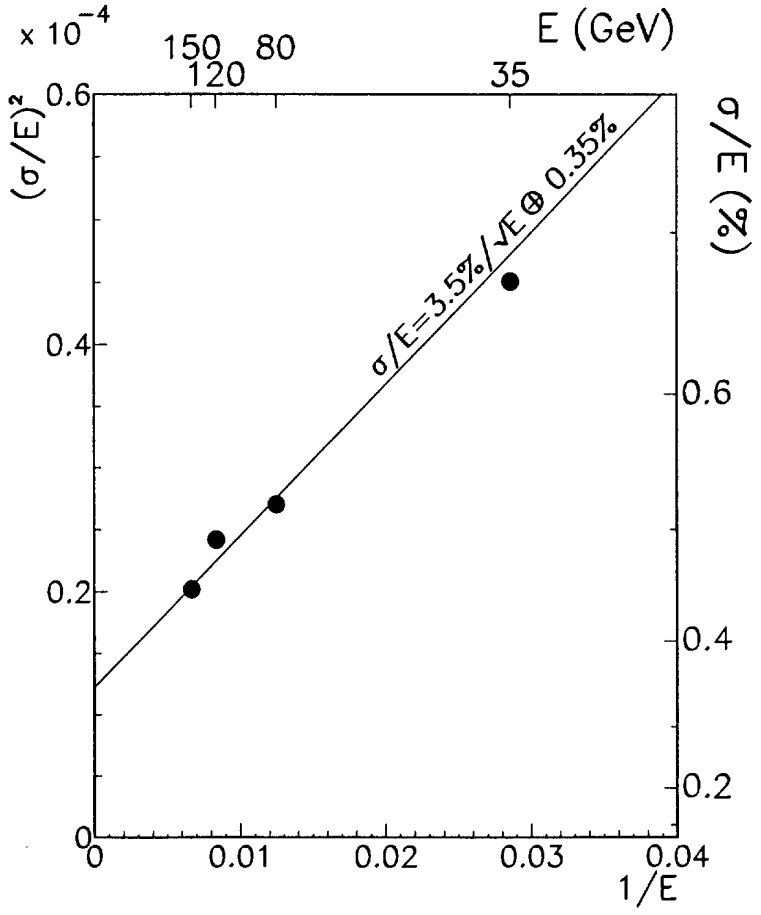

Fig. 15

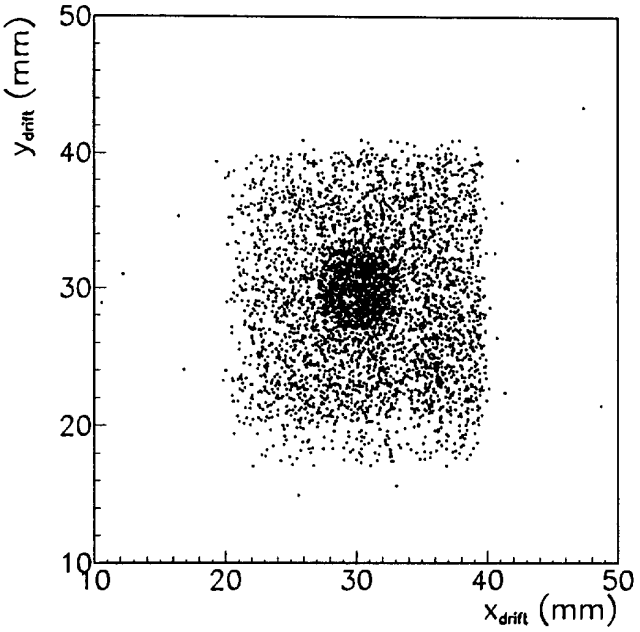
y_{drift} (mm)
50
40
30
20
10
10
20
30
40
50
x_{drift} (mm)

Fig. 16

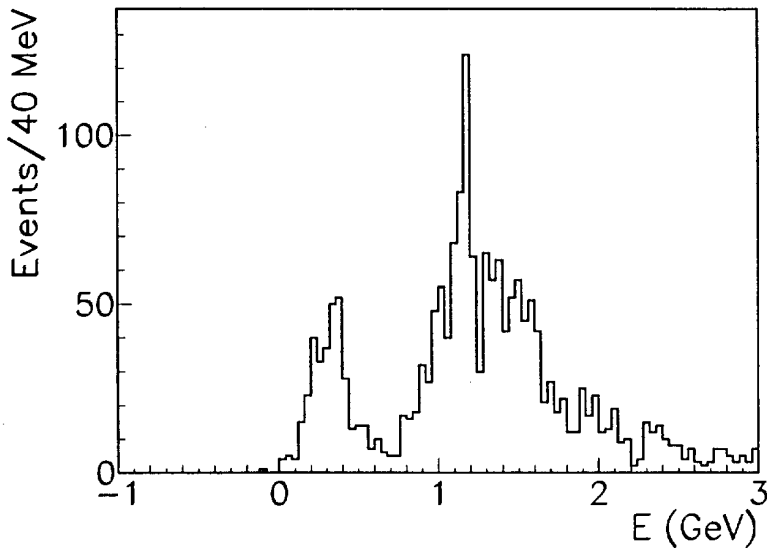
Events/40 MeV
100
50
0
−1
0
1
2
3
E (GeV)

Fig. 17

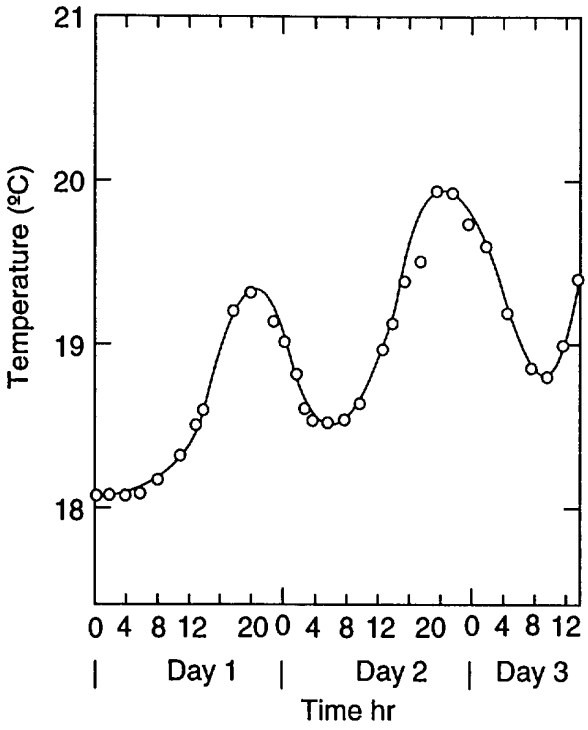
21
20
19
18
Temperature (ºC)
0 4 8 12 20 0 4 8 12 20 0 4 8 12
Day 1
Day 2
Day 3
Time hr

Fig. 18

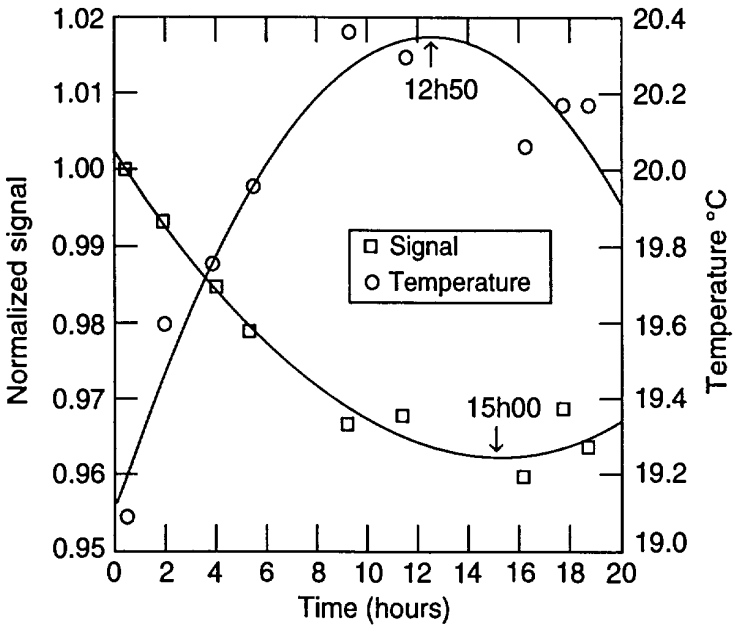
1.02
1.01
1.00
0.99
0.98
0.97
0.96
0.95
Normalized signal
20.4
20.2
20.0
19.8
19.6
19.4
19.2
19.0
Temperature °C
12h50
15h00
Signal
Temperature
0 2 4 6 8 10 12 14 16 18 20
Time (hours)

Fig. 19

a)

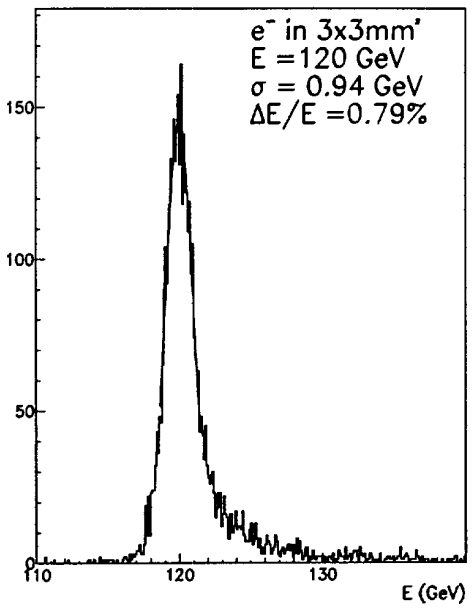

b)

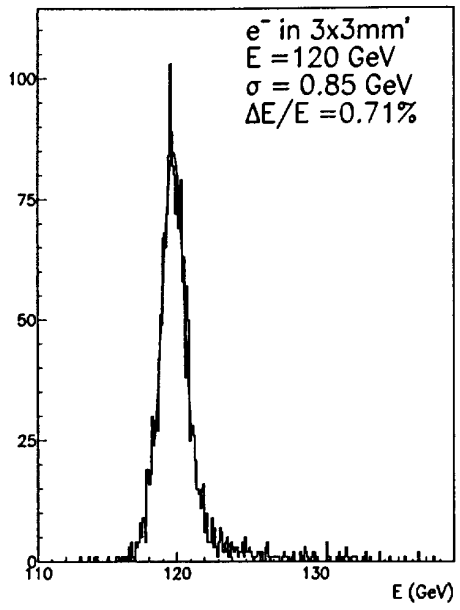

Fig. 20

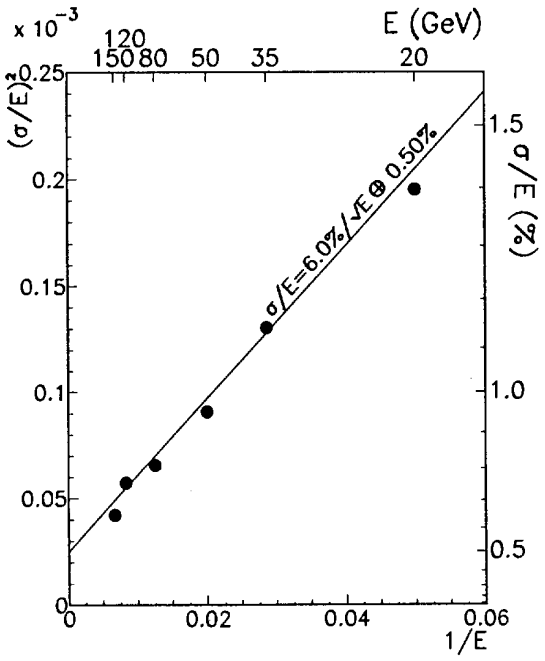

Fig. 21

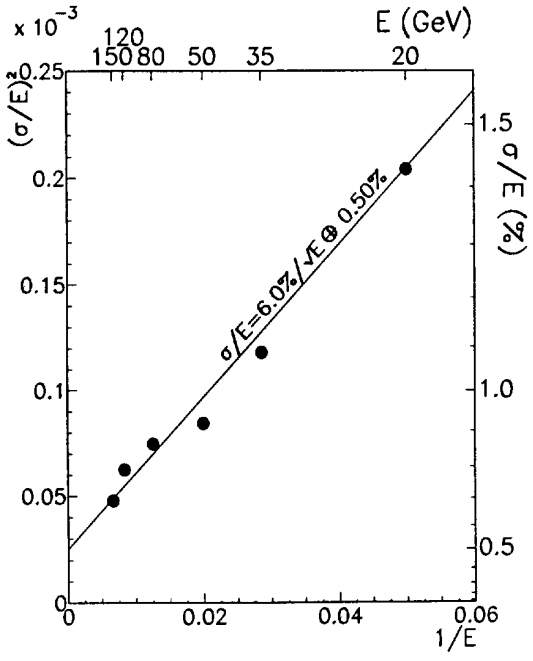

Fig. 22

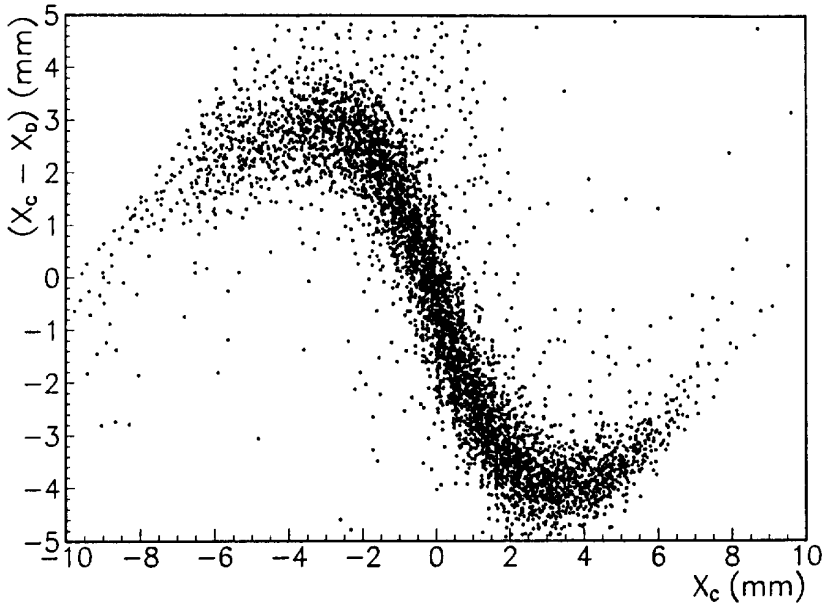
$(X_c - X_D)$ (mm)
X_c (mm)

Fig. 23

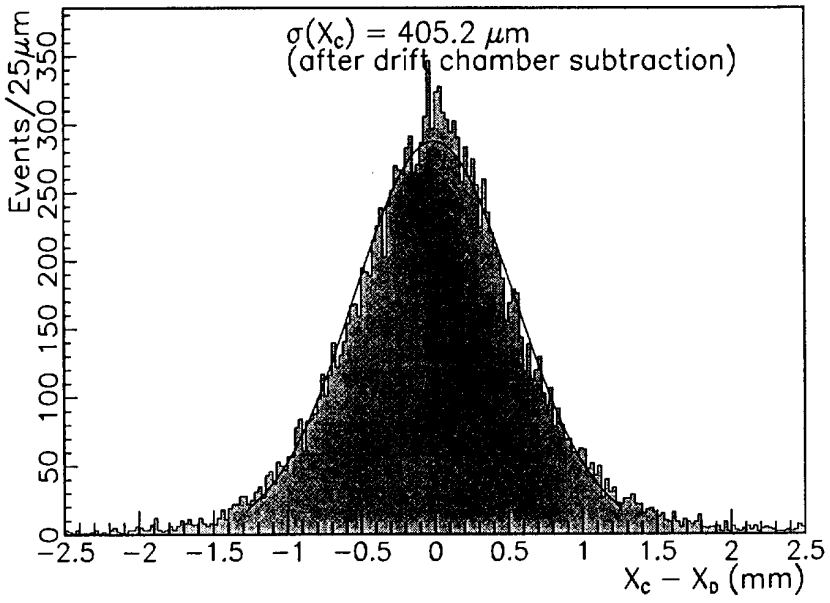
$\sigma(X_c)$ = 405.2 μm
(after drift chamber subtraction)
Events/25μm
$X_c - X_D$ (mm)

Fig. 24

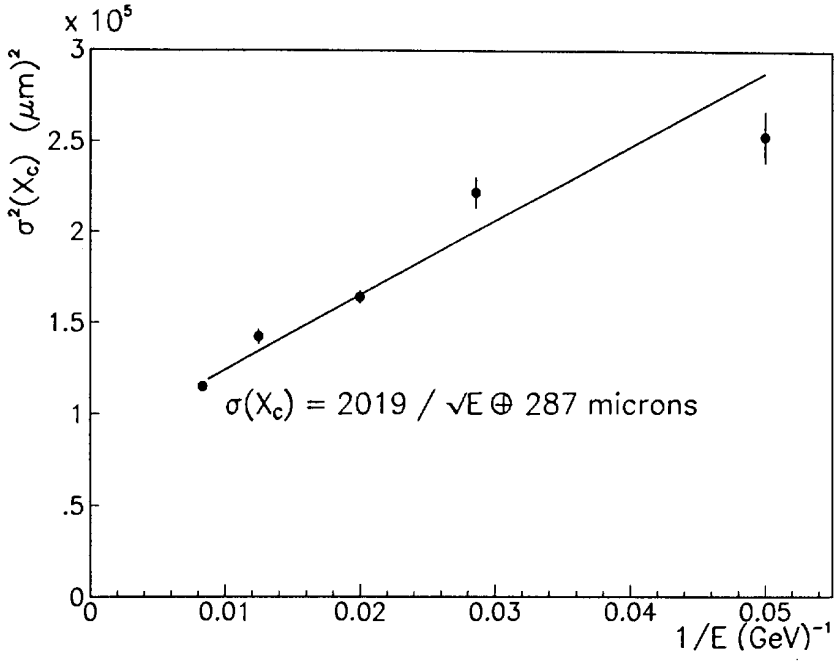
x 10^5
σ²(X_c) (μm)²
3
2.5
2
1.5
1
.5
0
0
0.01
0.02
0.03
0.04
0.05
1/E (GeV)^-1
σ(X_c) = 2019 / √E ⊕ 287 microns

Fig. 25

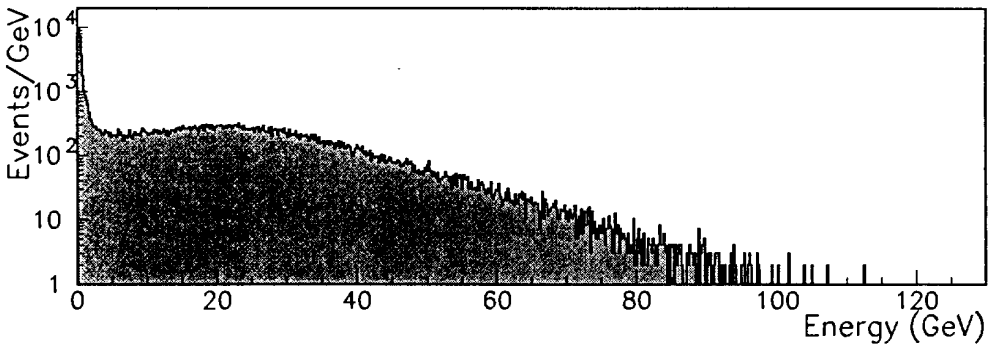
Events/GeV
10^4
10^3
10^2
10
1
0
20
40
60
80
100
120
Energy (GeV)

Fig. 26

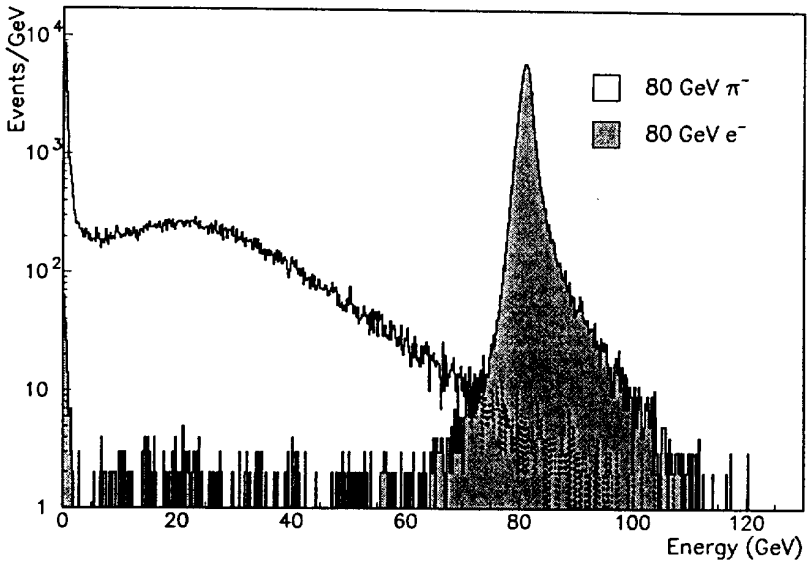
Events/GeV
10^4
10^3
10^2
10
1
0
20
40
60
80
100
120
Energy (GeV)
80 GeV π^-
80 GeV e^-

Fig. 27

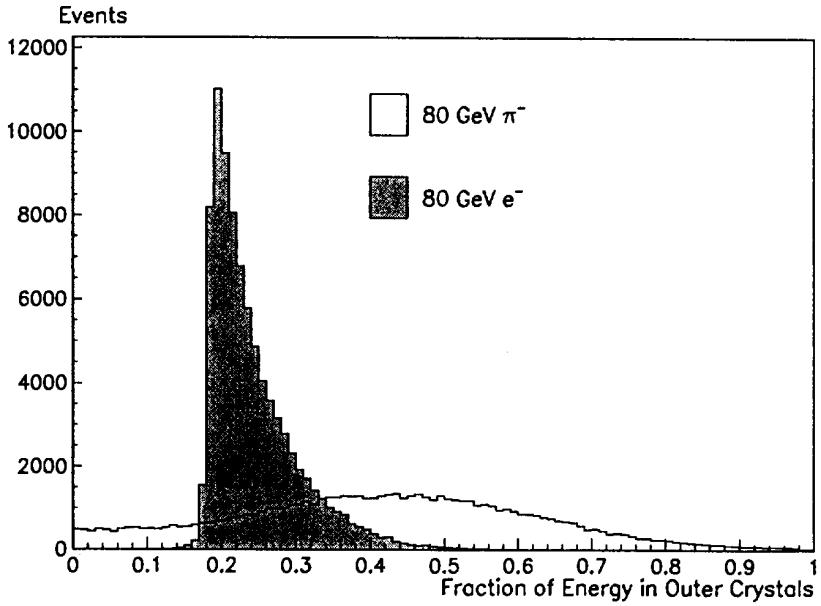
Events
12000
10000
8000
6000
4000
2000
0
0
0.1
0.2
0.3
0.4
0.5
0.6
0.7
0.8
0.9
1
Fraction of Energy in Outer Crystals
80 GeV π^-
80 GeV e^-

Fig. 28

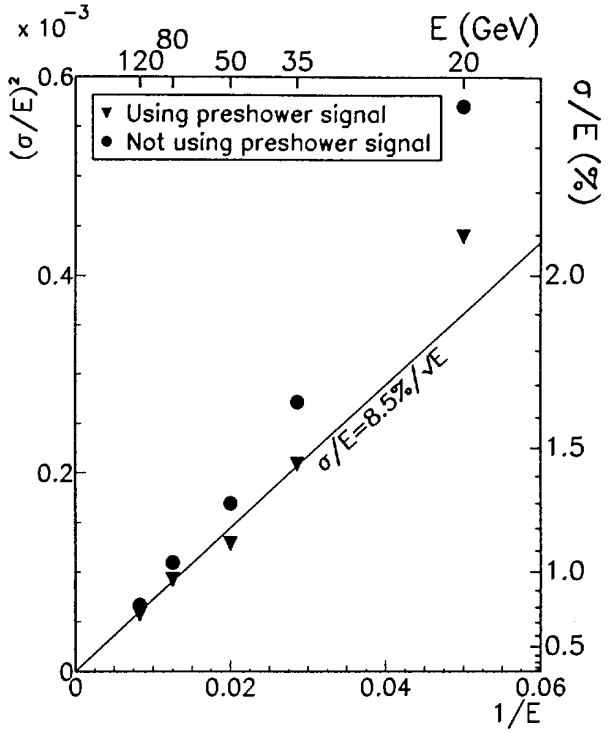
x 10^-3
E (GeV)
120
80
50
35
20
(σ/E)²
σ/E (%)
Using preshower signal
Not using preshower signal
σ/E=8.5%/√E
0.6
0.4
0.2
0
2.0
1.5
1.0
0.5
0.02
0.04
0.06
1/E

Fig. 29

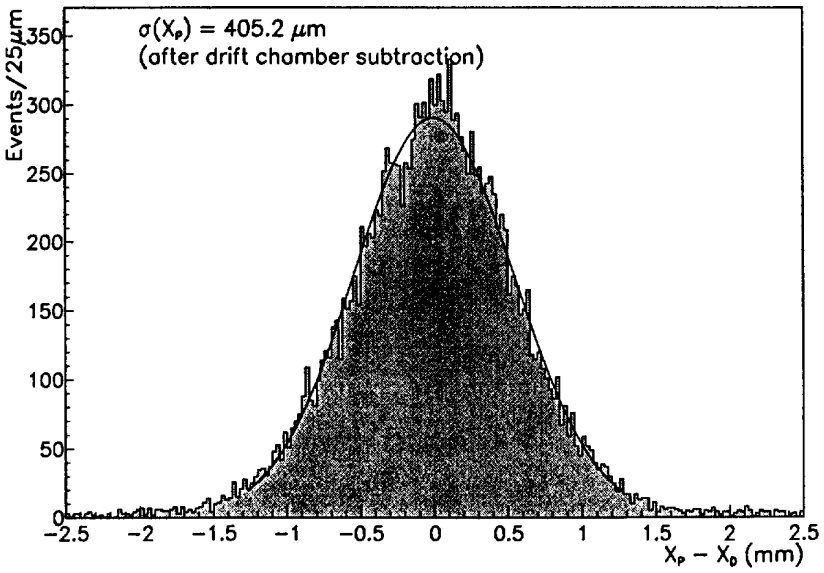
σ(X_p) = 405.2 μm
(after drift chamber subtraction)
Events/25μm
350
300
250
200
150
100
50
0
−2.5
−2
−1.5
−1
−0.5
0
0.5
1
1.5
2
2.5
X_p − X_0 (mm)

Fig. 30

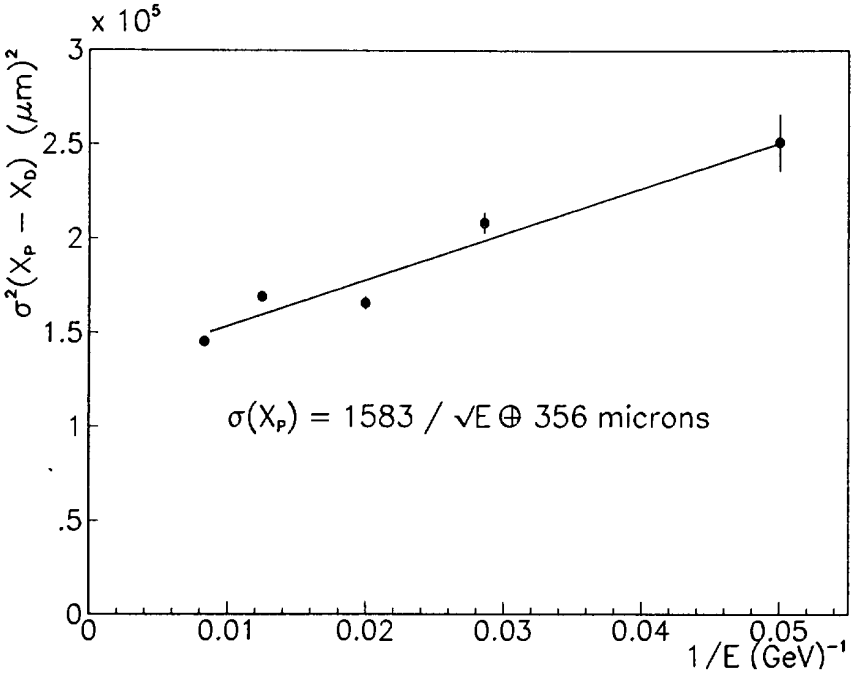
x 10⁵
σ²(X_P − X_D) (μm)²
σ(X_P) = 1583 / √E ⊕ 356 microns
1/E (GeV)⁻¹

Fig. 31

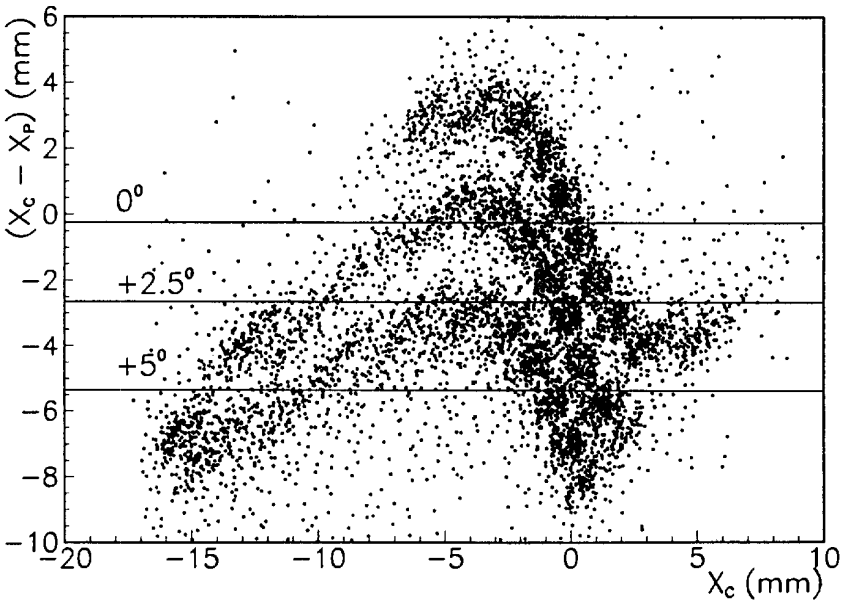
(X_C − X_P) (mm)
0°
+2.5°
+5°
X_C (mm)

Fig. 32

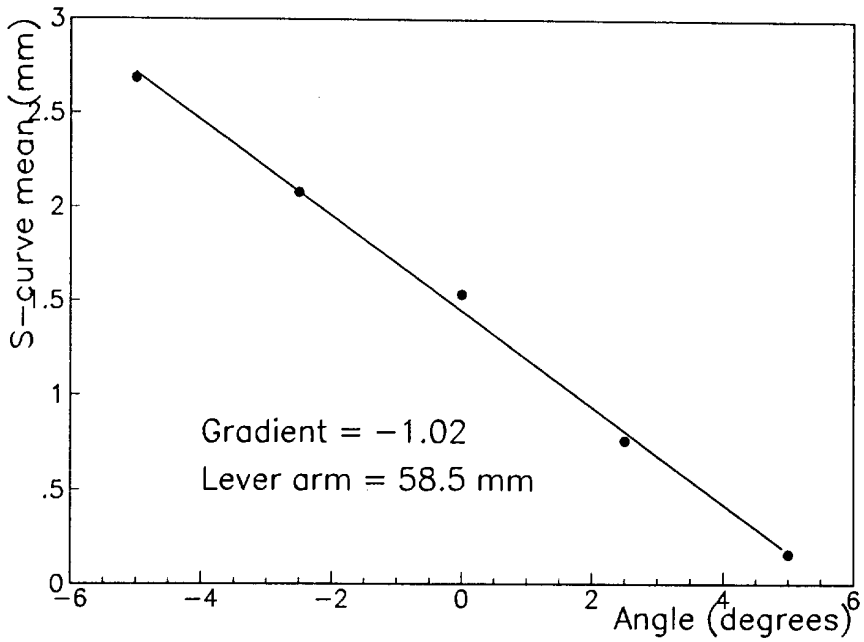
S−curve mean (mm)
Gradient = −1.02
Lever arm = 58.5 mm
Angle (degrees)

Fig. 33

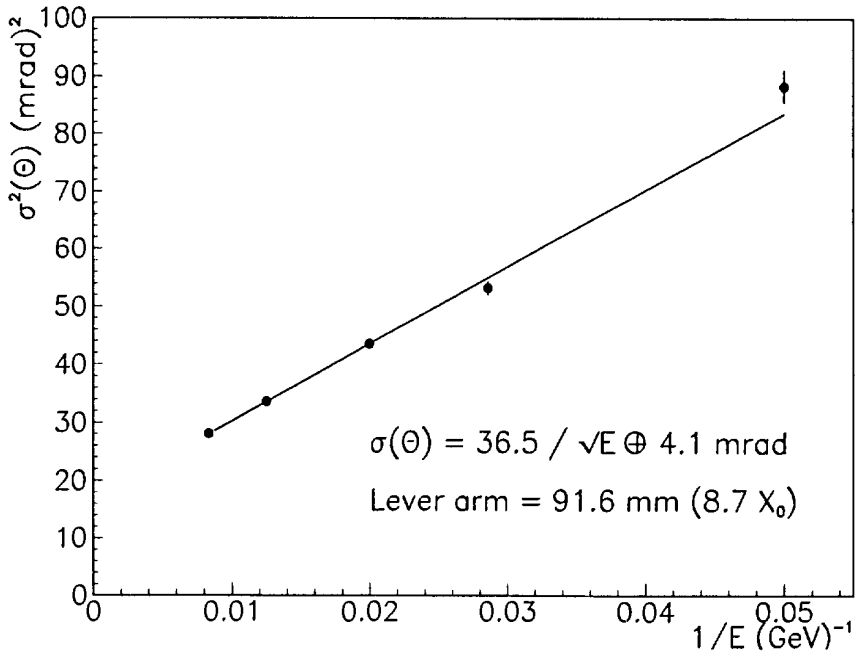
σ²(Θ) (mrad)²
σ(Θ) = 36.5 / √E ⊕ 4.1 mrad
Lever arm = 91.6 mm (8.7 X₀)
1/E (GeV)⁻¹

Fig. 34